ADVANCED MATERIALS INTERFACES
Open Access
www.advmatinterfaces.de

Enhancing the Photocatalytic Activity by Tailoring an Anodic Aluminum Oxide Photonic Crystal to the Semiconductor Catalyst: At the Example of Iron Oxide

Carina Hedrich, Anna R. Burson, Silvia González-García, Víctor Vega, Victor M. Prida, Abel Santos, Robert H. Blick, and Robert Zierold**

Photonic crystals (PhCs) are interesting structures for photocatalytic applications because of their capability of harnessing distinct forms of light–matter interactions within the PhCs. Of all these, overlapping one of the photonic stopband's (PSB) edge with the absorption of the PhC material or adsorbed molecules improves their excitation and generated charge carriers can subsequently induce photocatalytic reactions. The PSB position of anodic aluminum oxide PhCs (AAO-PhCs) can be easily adjusted by modifying the anodization profile. Herein, AAO-PhCs are designed to match the band gap of a model semiconductor enabling a general photocatalytic activity enhancement independent of the chemical to be decomposed. Fe_2O_3, as an example photocatalyst, is coated onto AAO-PhCs to demonstrate efficient photocatalytic systems by utilizing the slow photon effect. Tailored Fe_2O_3-AAO-PhCs with their PSB edge at 564 nm matching the Fe_2O_3 band gap exhibit generally enhanced degradation of three different organic dyes while a significant activity decrease is observed when the PSB edge does not overlap with the Fe_2O_3 absorption. Furthermore, photocatalyst degradation can be reduced down to only 4% activity loss over six consecutive measurements by an ultra-thin alumina coating.

1. Introduction

Purification of water is particularly important nowadays to ensure the supply of drinking water to society, especially in light of major challenges such as climate change and overpopulation.[1,2] Access to drinking water has been defined as Sustainable Development Goal (SDG) number 6 by the United Nations.[3] Thus, cheap, reusable, sustainable, and decentralized water purification systems are urgently needed. Photocatalysts came into focus over the last decades as they use sunlight to induce chemical reactions, e.g., degradation of various pollutants in water.[4–8]

Since the discovery of photocatalysis, titanium dioxide (TiO_2) has become the benchmark photocatalytic material due to its availability, inertness, stability, and good photocatalytic properties in different processes.[9–12] However, it

C. Hedrich, A. R. Burson, R. H. Blick, R. Zierold
Center for Hybrid Nanostructures
Universität Hamburg
22761 Hamburg, Germany
E-mail: carina.hedrich@chyn.uni-hamburg.de;
robert.zierold@chyn.uni-hamburg.de

S. González-García, V. M. Prida
Physics Department
School of Sciences
University of Oviedo
Oviedo, Asturias 33007, Spain

V. Vega
Laboratory of Nanoporous Membranes (SCTs-Severo Ochoa)
University of Oviedo
Oviedo, Asturias 33006, Spain

A. Santos
School of Chemical Engineering
The University of Adelaide
Adelaide, SA 5005, Australia

A. Santos
Institute for Photonics and Advanced Sensing
The University of Adelaide
Adelaide, SA 5005, Australia

R. H. Blick
Material Science and Engineering
College of Engineering
University of Wisconsin-Madison
Madison, WI 53706, USA

The ORCID identification number(s) for the author(s) of this article can be found under https://doi.org/10.1002/admi.202300615

DOI: 10.1002/admi.202300615

suffers from insufficient use of the solar light spectrum since UV light—which is only 5–10% of the sunlight spectrum at the Earth's surface—is required to initiate photocatalytic processes in TiO_2.[13] Besides strategies to tune the excitation of TiO_2 toward the visible range such as doping or creation of oxygen vacancy defects,[14] other photocatalytically active materials, namely various oxides, sulfides, and nitrides, or combinations among them are also intensively studied.[6,7,15–19] Iron (III) oxide (hematite, Fe_2O_3), for example, is a promising photocatalyst because it is abundant on Earth and its electronic band gap is located in the visible region of the electromagnetic spectrum (≈1.7–3.1 eV).[17,20,21] Accordingly, irradiance-rich sunlight spectral regions can be harvested to excite iron oxide and thereby induce photocatalytic reactions such as oxidative water purification. Moreover, Fe_2O_3 is a non-toxic material, which could be applied in the decontamination of drinking water. Nevertheless, the generation of charge carriers in Fe_2O_3 is often inefficient or the fast charge carrier recombination prevents the induction of reactions by the charge carrier.[22–24] To overcome this limitation, combining Fe_2O_3 with other semiconductors to form heterojunctions has been demonstrated as an approach to improve charge carrier separation.[22,25,26] Alternatively, engineering light–matter interactions between incoming light and Fe_2O_3 by tailoring the structure of the semiconductor also provides an effective means of increasing the generation yield of charge carriers. This approach also applies to many other semiconductors featuring low charge carrier generation rates. For example, the so-called slow photon effect in photonic crystals (PhCs) can be rationally engineered for this purpose.[27–29]

PhCs are structures composed of periodically arranged materials with different dielectric constants. These periodic variations within the structures result in photonic stopbands (PSBs)—also denoted as photonic band gaps—wherein photons with the respective wavelength cannot propagate through the PhC and are therefore reflected at the PhC's surface.[30-33] At the blue and red edges of the PhC's PSB, the group velocity of photons is strongly reduced, which is referred to as the slow photon effect (**Figure 1**a). These photons have more time to interact with the PhC material and thus, the interaction probability between incident photons and atoms of the material is increased.[27,28,34] Consequently, charge carrier generation in semiconductor-based PhCs can be enhanced by utilizing the slow photon effect when one edge of the PSB is aligned with the electronic band gap of the semiconductor. PhCs can be realized in one, two, or three dimensions.[31,32] Especially two- and three-dimensional PhCs are interesting for photocatalytic applications because they can consist of porous structures that provide high surface areas and, accordingly, many possible reaction sites. The most common semiconductor-based three-dimensional PhC structures are inverse opals, which are characterized by a semiconductor matrix around hollow spheres.[12,27,28,34-36] However, PhCs can also be fabricated by tailoring the anodization of aluminum.[37-40] Anodic aluminum oxide (AAO) structures consist of cylindrical, self-organized, highly ordered pores inside electrochemically prepared aluminum oxide. The pores of AAO feature distinct geometrical parameters, namely pore diameter, interpore distance, and pore length, which can be adjusted by tuning the electrochemical anodization parameters.[39,41-43] Specifically, the application of pulse-like anodization approaches modifies the pore morphology from straight to periodically diameter-modulated structures (Figure 1b). Such modulated structures act as PhCs and their PSB can be precisely tailored across the UV to IR spectral range through judicious input anodization parameters.[37-40]

On the one hand, tuning the PSB position of semiconductor-functionalized AAO-PhCs to overlap the PSB edge with the absorption wavelength of chemical pollutants boosts the photodegradation efficiency of these platforms.[29,44-46] The photocatalytic activity of such tailor-made aligned AAO-PhCs is enhanced by the slow photon effect for the specific chemical, but it decreases when the photocatalytic decomposition of compounds with absorption bands off-side the PSB edge is tested. In the latter case, the slow photon effect no longer enhances the activity because the PSB edge is misaligned with the compounds' absorption maximum.

On the other hand, Liu et al. reported an enhanced photocatalytic degradation of organic dyes serving as model water pollutants when the PSB edge matches the band gap of TiO_2, which was coated onto the AAO-PhC structure by sol–gel chemistry. However, TiO_2 excitation requires irradiation by UV light. To use the visible range of the electromagnetic spectrum, a semiconductor with a fitting band gap must be employed to increase the photocatalytic activity of a functionalized AAO-PhC. Thus, Fe_2O_3 is utilized in this study as a photocatalytically active semiconductor featuring a band gap in the visible region.[23,24]

Ideal photocatalysts for purification systems should be durable, meaning they can be utilized multiple times without significant loss of their photocatalytic activity.[4,52] Altering and destruction of Fe_2O_3 upon irradiation, and consequently, a corresponding reduction of their photocatalytic performance is often observed for this photocatalyst material.[11,53,54] This phenomenon is denoted as photocorrosion or photodissolution since structural changes and decomposition processes of the Fe_2O_3 are induced by the illuminating (solar) light applied in photocatalytic processes to excite the semiconductor. Hence, the photocatalyst surface has to be protected to avoid such degradation, which could, for example, be realized by coating ultra-thin layers of metal oxides on top of the Fe_2O_3 film.[11,53–60]

Apart from the PSB edge alignment with the semiconductor band gap, the film thickness of the semiconductor might be crucial for optimizing the photocatalytic performance of semiconductor-coated AAO-PhCs because it determines the charge carrier dynamics within the semiconductor as well as the mass transfer of photocatalytic reactants within the pores.[11,20,22-24] Specifically, the minority charge carrier diffusion length in Fe_2O_3 is only a few nanometers[20] whereby a low film thickness of Fe_2O_3 is therefore beneficial to achieve high photocatalytic activities. On the contrary, thicker films of at least a few tens of nanometers are required to ensure complete absorption of the incident sunlight by Fe_2O_3.[20,47] Tailor-made functionalized AAO-PhCs provide new opportunities to balance these opposing effects by structural engineering of the nanostructure. Fe_2O_3 thin films deposited in the pores possess low thicknesses in the radial direction of the pores (i.e., diameter) while they cover a few tenths of micrometers in the pores' axial direction (i.e., length). Herein, atomic layer deposition (ALD) of Fe_2O_3 is applied to enable precise control over the deposited film thickness on the sub-nanometer scale.[48-51] Accordingly, ALD is well-suited as a functionalization technique to develop composite

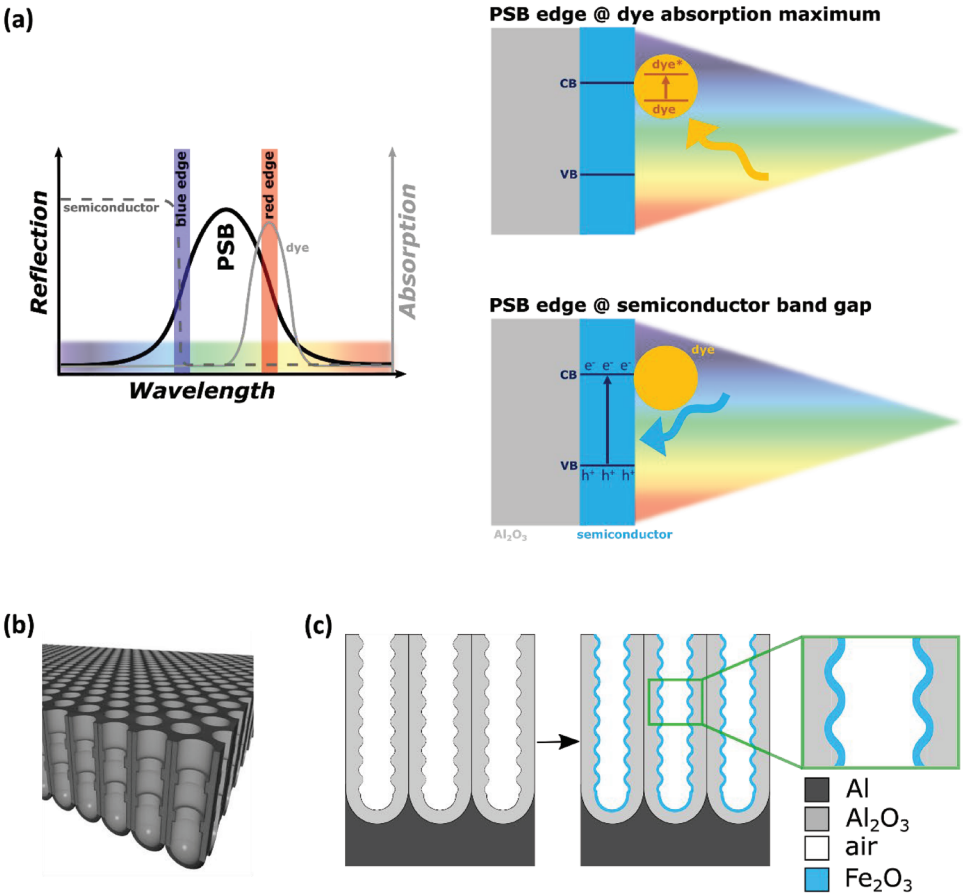

Figure 1. Schematic of photonic crystals, their optical properties, and the construction of Fe_2O_3-functionalized anodic aluminum oxide photonic crystals. a) Due to the periodic modulation of the refractive index, a PhC exhibits a photonic stopband (PSB) which does not allow light propagation of specific wavelengths within the structure. Incoming light of this spectral region is reflected at the samples' surface. Due to the slow photon effect, light–matter interactions within the PhC are increased at the blue and red edges of the PSB (marked in the scheme). The position of the PSB edges can be tuned by controlling the preparation process to overlap with either the absorption of a dye (continuous grey line) or with the band gap of a semiconductor (dashed grey line), corresponding to the red and the blue edge, respectively. Depending on this alignment, the slow photon effect enhances the light absorption within the PhC structure by accelerating the excitation of the dye (upper right scheme) or of the semiconductor (lower right scheme). b) An AAO-PhC is exemplarily shown, featuring periodic diameter modulations of the pores. c) The AAO-PhC template is fabricated by pulse-like anodization of aluminum. Herein, the structures' surface is subsequently coated via atomic layer deposition of Fe_2O_3.

semiconductor–AAO PhCs to study the photocatalytic performance of the structure with respect to the Fe_2O_3 film thickness.

In this work, we demonstrate how the photocatalytic activity of Fe_2O_3 coatings in structurally engineered AAO-PhCs can be enhanced by making use of the slow photon effect when the structures' PSB edge is aligned with the band gap of the semiconductor. Fe_2O_3-AAO-PhCs are prepared by pulse-like anodization of aluminum and subsequent ALD coating of Fe_2O_3 with different thicknesses (Figure 1c). Moreover, ultra-thin aluminum oxide (Al_2O_3) layers are also deposited onto optimized Fe_2O_3-AAO-PhCs by ALD to avoid photocorrosion and extend the lifetime of the semiconductor over repeated photocatalytic cycles. Fe_2O_3-AAO-PhCs' optical properties are characterized by UV–vis reflection measurements, and the photocatalytic performances are assessed with respect to the Fe_2O_3 film thickness. Specifically, Fe_2O_3-AAO-PhCs are immersed into aqueous solutions of model organic dyes—methylene blue (MB), rhodamine B (RhB), and methyl orange (MO)—and irradiated by visible light to analyze their photocatalytic degradation of the dyes. The structures' PSB characteristics and Fe_2O_3 film thicknesses are related to photocatalytic performances.

2. Results and Discussion

2.1. Fabrication and Optical Characterization of AAO-PhCs

AAO-PhCs with PSB edges located at wavelengths that match the Fe_2O_3 band gap are produced by applying rectangular current density pulses during the electrochemical oxidation of aluminum in oxalic acid ($H_2C_2O_4$, 0.3 M) electrolyte, as shown in **Figure 2**. The voltage signal response (output) of the aluminum chip anodized under these conditions follows the rectangular current density pulses with distortion of the pulse shape. The output pulses resemble a capacitor response with increase and decrease that follows the input current density with a certain temporal delay due to the recovery process of the barrier layer oxide at the

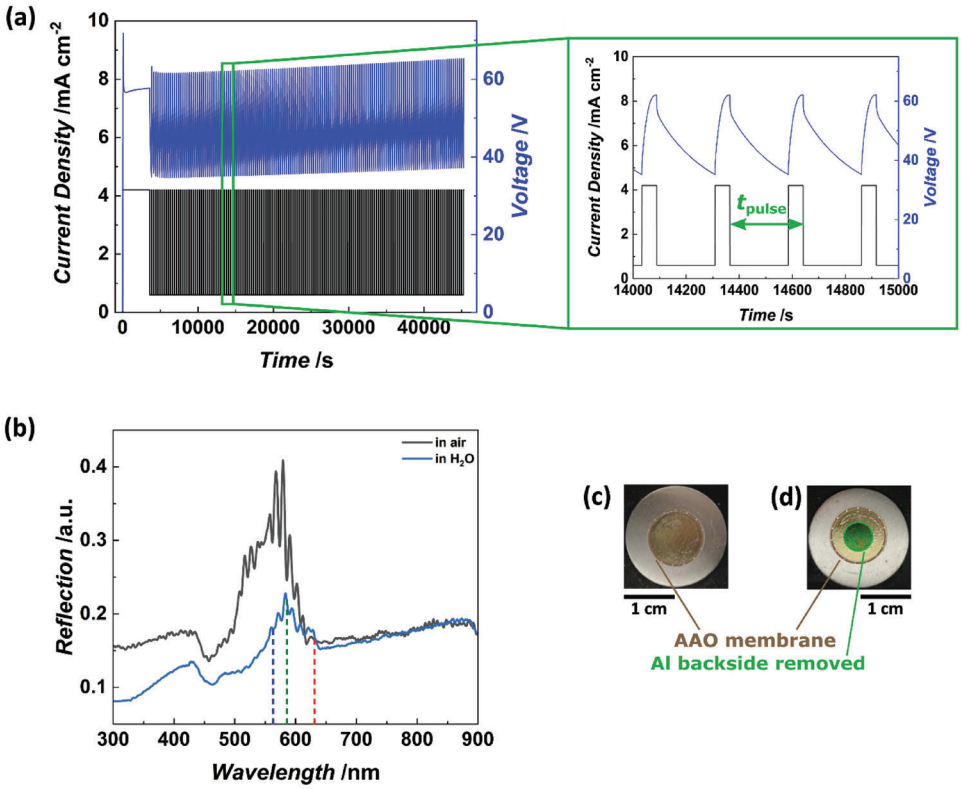

Figure 2. Fabrication and characterization of AAO-PhCs by pulse-like anodization in oxalic acid. a) Rectangular current pulses are applied to the aluminum chip after an initial constant current period. The voltage at the sample follows the pulse behavior with distortion of the pulse shape due to the recovery effects of the barrier oxide layer. b) UV–vis reflection measurements reveal the PSB position of AAO-PhCs. The PSB position redshifts when the pores are infiltrated with H_2O compared to air due to the increased refractive index of the medium. The dashed lines indicate the positions of the PSB maximum (green line), the PSB blue edge (blue line), and the PSB red edge (red line). The PSB maximum is obtained by a Gaussian fit of the data, while the PSB edges are defined as the inflection points of the reflection peak. c,d) Photographs of the AAO-PhC samples. The AAO sample is indicated by the brown dotted circle. The aluminum backside of the sample is wet-chemically removed in (d), whereby the green color in reflection becomes visible.

bottom side of the nanopores (i.e., growth front of the anodic film).[61-64] Moreover, the pulses are also asymmetric in shape. These pulses result in the formation of gradient-index filter-like structures, which are characterized by a smooth variation of pore diameter in depth (scanning electron microscope (SEM) images are shown in Figure S1, Supporting Information).[29,65,66] Such AAO structures exhibit PSBs in the visible light range, as exemplarily shown in Figure 2b. The PSB position is determined by the pulse period (t_{pulse}) and undergoes a red shift when the pores are infiltrated with water (H_2O) compared to air. The increment of the refractive index of the pore-filling medium (i.e., change from air to H_2O)[67] leads to an increment of the effective refractive index of the filled AAO structure and simultaneous reflection intensity decrease. Analysis of the PSB properties is shown for the measurement in H_2O by the dashed lines. The blue line indicates the PSB blue edge, the red line resembles the PSB red edge, and the green line is the position of the PSB maximum (i.e., its maximum in intensity). Note, the inflection points of smoothed reflection data are calculated as the PSB edges ($\lambda_{PSB,blue}$; $\lambda_{PSB,red}$), while the peak maximum wavelength of a Gaussian fit defines the PSB maximum position λ_{PSB}. When the aluminum backside of the AAO-PhCs sample is present (Figure 2c), samples produced with t_{pulse} = 275 s appear yellow in an optical photograph. When the aluminum backside of the underlying chip is removed, the refractive index contrast between the AAO-PhC and the background is higher and the green color reflected by the structures' PSB becomes visible, as demonstrated in Figure 2d.

Tuning t_{pulse} in the anodization or coating the samples with different thicknesses of Fe_2O_3 by ALD after their production modifies the PSB positions. Since the photocatalytic performance of semiconductor-modified AAO-PhCs is assessed in an aqueous medium, the structures' optical properties are characterized when the pores are infiltrated with deionized water (DI-H_2O). **Figure 3**a depicts the reflection spectra of as-produced, DI-H_2O-infiltrated AAO-PhCs fabricated with t_{pulse} of 175, 270, 275, 300, 335, and 450 s, respectively. Note, the PSB characteristics are denoted as λ_{PSB} ($\lambda_{PSB,blue}$; $\lambda_{PSB,red}$), where the PSB maximum wavelength λ_{PSB} is calculated by a Gaussian fitting while the inflection points of the PSB define the blue ($\lambda_{PSB,blue}$) and red edges ($\lambda_{PSB,red}$). Here, the λ_{PSB} and the PSB edges change from 455 nm ($\lambda_{PSB,blue}$ = 428 nm; $\lambda_{PSB,red}$ = 477 nm) up to 858 nm (844 nm; 883 nm) with increasing pulse duration (Figure 3b) at a measured average rate of 1.5 ± 0.1 nm s^{-1}. Since the reflection intensity of the samples applied in the photocatalysis measurements in this study (fabricated with t_{pulse} = 270 s and t_{pulse} = 275 s) are in the same absolute range, an effect of the PSB reflection intensity

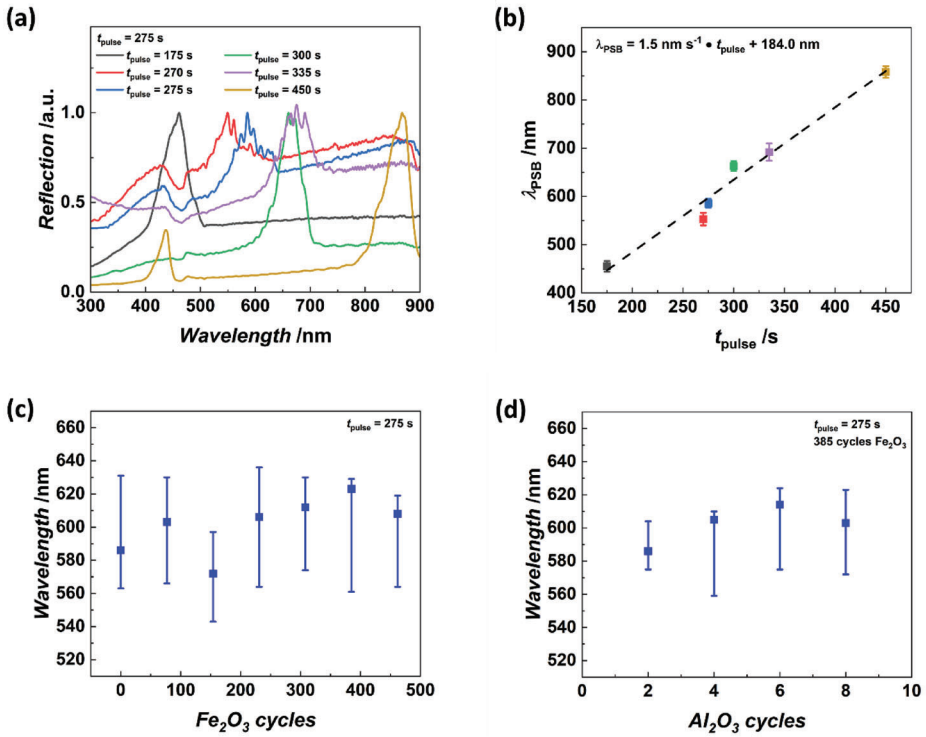

Figure 3. Optical properties of AAO-PhCs anodized by applying different pulse durations and coated with Fe_2O_3 by ALD after production. a) Normalized reflection spectra of samples anodized with varying pulse durations show a red shifting of the PSB position upon increasing the pulse duration. b) The PSB maximum wavelength depends linearly on the applied pulse duration t_{pulse} with a slope of 1.5 ± 0.1 nm s^{-1}. The error of the fit is 0.97. c) The PSB position is almost independent of the applied ALD cycle number for AAO-PhCs anodized with tpulse = 275 s and subsequently coated with Fe_2O_3 by ALD Here, the error bars denote the blue and red edge of the PSB while the data point represents the PSB maximum position λ_{PSB}. d) Depositing ultra-thin Al_2O_3 layer on AAO-PhCs prepared with 275 s pulse duration and previously coated by 385 cycles Fe_2O_3 does not significantly influence the PSB positions. (Reflection spectra for the samples characterized in (c,d) are shown in Figure S3 (Supporting Information).

on the photocatalytic performance for comparing the samples is herein not expected.

The PSB maximum wavelength and the blue and red edge of AAO-PhCs produced by 275 s pulse duration and coated with different cycle numbers of Fe_2O_3 by ALD are shown in Figure 3c. Within one Fe_2O_3 ALD cycle, 0.016 ± 0.003 nm Fe_2O_3 are deposited and, accordingly, the applied ALD cycle numbers of 0, 77, 154, 231, 308, 385, and 462 cycles correspond to nominal film thicknesses of 0, 1, 2, 3, 4, 5, and 6 nm Fe_2O_3, respectively. Thicknesses of ALD-deposited films were analyzed by spectral ellipsometry on planar silicon reference substrates (Figure S2, Supporting Information). The AAO-PhCs exhibit similar PSB properties after ALD coating with a few nm of Fe_2O_3 and an overcoating by an ultra-thin aluminum oxide layer (Figure 3d), all in the range of the error obtained during AAO-PhC fabrication. Analysis of the AAO-PhCs' optical properties reveals that the PSB edges of samples coated with 77, 231, 385, and 462 Fe_2O_3 cycles by ALD overlap with the electronic band gap of Fe_2O_3 of ≈2.2 Ev,[23,24] which corresponds to a wavelength of ≈564 nm. Here, a specific wavelength value is given for each PSB edge, whereby the "edge" region, which is essential for the slow photon effect, extends over a few nanometers. In Figure S3 (Supporting Information), the influence of Fe_2O_3 and Al_2O_3 coating on the PSB characteristics of AAO-PhCs fabricated with pulse durations of 270 and 335 s are shown compared to uncoated samples.

AAO-PhCs produced with similar pulse-like anodization approaches have previously been reported in literature.[29,40,44–46,61,64–86] These structures show different PSB characteristics, namely position, width, intensity, and shape, depending on the anodization conditions. The herein presented profile utilizing rectangular current pulses in $H_2C_2O_4$ leads to similar AAO-PhCs as the existing approaches regarding the PSB reflection intensity and width. For example, reflection intensities reported in literature vary between 10% and 95%, depending on the applied conditions, while full width at half-maximum (FWHM) values from 16 nm up to 202 nm are observed.[65,67,73,81,82]

To functionalize AAO-PhCs produced in $H_2C_2O_4$ with a photocatalytic active material, in literature the structures were coated with TiO_2 by sol–gel chemistry.[29,44,45,80,85] It was reported that the coating red-shifted the PSB position of the samples due to the higher refractive index of TiO_2 compared to that of anodic Al_2O_3.[29,80] Furthermore, the coating reduced the AAO-PhC pore diameter, which induced a red shift of the PSB position. In 2021, Lim et al. deposited thin layers of TiO_2 onto AAO-PhCs by ALD, with film thicknesses below 2 nm. Since the thicknesses are much lower and better controlled than for sol–gel deposition processes, none of these samples significantly shifted the PSB position. Similarly, herein only slight shifts of the PSB positions were observed for AAO-PhCs anodized with pulse durations of

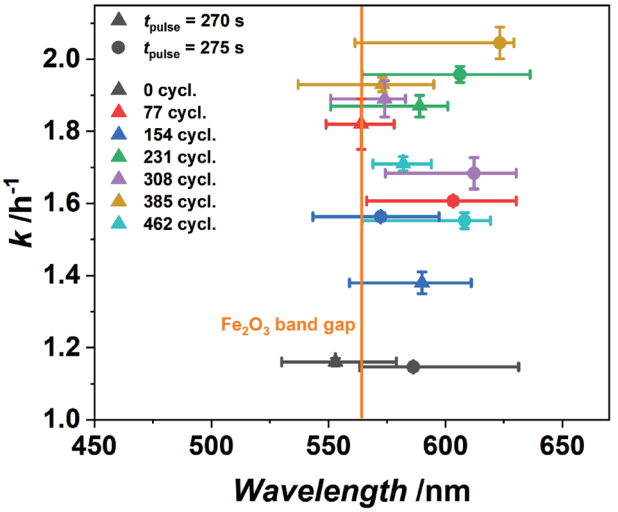

Figure 4. Photocatalytic performances of Fe_2O_3-AAO-PhCs functionalized by different ALD cycle numbers. The photocatalytic activity depends on the pulse duration applied in anodization and the number of Fe_2O_3 cycles of the ALD process. For both AAO-PhC types anodized with different pulse durations t_{pulse}, the deposited Fe_2O_3 film thickness in combination with the PSB characteristics determines the photocatalytic performance. Analysis of the PSB edge positions with respect to the Fe_2O_3 band gap reveals that the highest activity is achieved when the PSB blue edge overlaps with the semiconductor band gap due to the slow photon effect. Note that the AAO-PhC coated by 385 ALD cycles for both sample types is most effective in photocatalytically degrading MB.

270, 275, and 335 s after coating with iron oxide and/or Al_2O_3 by ALD.

2.2. Photocatalytic Activity of Fe_2O_3-AAO-PhCs

The photocatalytic performance of Fe_2O_3-functionalized AAO-PhCs with PSB edges located in the region of the Fe_2O_3 band gap depends on the Fe_2O_3 ALD cycle numbers. The Fe_2O_3 thickness, which corresponds to the different ALD cycles, is known to affect the charge carrier generation and recombination.[11] For Fe_2O_3-AAO-PhCs produced by 270 s pulse duration within anodization, the photocatalytic activity of MB degradation is the lowest (1.38 ± 0.03 h^{-1}) for 154 ALD cycles, while the highest activity of 1.93 ± 0.02 h^{-1} is observed for a sample coated with 385 cycles (**Figure 4**). As depicted in Figure 4, the alignment of the PSB edge with the Fe_2O_3 band gap is the best for the 385 ALD cycle sample, which shows the highest photocatalytic activity. However, the different photocatalytic performances depending on the ALD cycle numbers cannot be explained by only considering the PSB edge alignment to the Fe_2O_3 band gap. Instead, additional factors such as film thickness and surface roughness must be considered. It is reported in literature that the film thickness of semiconductors determines their charge carrier dynamics, i.e., charge carrier generation and recombination.[11] For Fe_2O_3, fast charge carrier recombination and low carrier mobility are common drawbacks to its application in photocatalytic processes.[22-24]

Apart from determining the charge carrier dynamics, the deposited film thickness also influences the mass transfer of molecules into and out of the pores of AAO-PhCs. The ALD-coated material narrows the pore diameter increasing the pores' aspect ratio. Thus, the diffusion of molecules taking part in the photocatalytic reaction within the pores gets increasingly constrained by the increasing ALD cycle number.[87–89] Hence, it is expected that this diffusion limitation leads to a decrease in the photocatalytic activity when a certain film thickness is reached. The surface roughness of our ALD-deposited Fe_2O_3 films decreases with increasing cycle number, as summarized in **Table 1**. The atomic force microscopy (AFM) images of the different films are shown in Figure S3 (Supporting Information). Nucleation of individual Fe_2O_3 islands occurs via the Volmer-Weber growth mechanism, which will grow together with increasing ALD cycle number, resulting in a continuous Fe_2O_3 layer.[48,90,91] Due to the higher roughness of 3.83 nm after 77 ALD cycles, the materials' surface area is higher for lower ALD cycle numbers meaning that more active surface sites are available for the photocatalytic reactions. Therefore, the photocatalytic activity is strongly increased for 77 Fe_2O_3 cycles compared to that of Fe_2O_3-functionalized AAO-PhCs with lower surface roughness. Interestingly, 154 ALD cycles still feature a higher surface roughness of 2.02 nm compared to that quantified in Fe_2O_3 films produced at higher cycle numbers (<1.55 nm), but this does not affect the photocatalytic reaction strongly.

Table 1. Characterization of surface roughness of Fe_2O_3 layers deposited by ALD with different cycle numbers. The silicon/ silicon dioxide wafers were coated in the same ALD processes as the AAO-PhCs.

ALD cycle number	Film thickness /nm	Surface roughness /nm
0	0	1.71
77	1	3.83
154	2	2.02
231	3	1.83
308	4	1.55
385	5	1.53
462	6	1.52

Taking all these effects (i.e., PSB edge alignment, charge carrier dynamics, diffusion limitation, and surface roughness) into account, the photocatalytic activities of all Fe_2O_3-functionalized AAO-PhCs produced with a pulse duration of 270 s can be mechanistically explained by the following: Application of 77 ALD cycles results in a photocatalytic activity of 1.82 ± 0.07 h^{-1} due to the high surface area of the Fe_2O_3 film caused by the large surface roughness of 3.83 nm. The influence of the surface area on the photocatalytic activity decreases with increasing ALD cycle number because the surface roughness—and thereby the available surface area—is reduced down to < 1.55 nm. For 154 cycles, the lowest activity of 1.38 ± 0.03 h^{-1} is observed. Note that the PSB edge is also not perfectly matched with the semiconductor band gap, contributing to the reduced effect. Further increasing the Fe_2O_3 cycles of the ALD process (231 and 308 cycles, respectively) results in an increased photocatalytic activity since the film thicknesses allow for more charge carrier generation without recombination, even though the optical properties are not optimized to make use of the slow photon effect. The highest activity of 1.93 ± 0.02 h^{-1} is observed for the sample coated by 385 cycles Fe_2O_3 because the film thickness seems to be optimal.

Specifically, enough charge carriers can be generated without recombination while mass transfer into and out of the pores is possible to a sufficient extent. A thicker Fe_2O_3 film (462 cycles) leads to reduced photocatalytic activity $1.71 \pm 0.02\ h^{-1}$, which might be attributed to a combination of different effects. First, the thicker film might not be optimal regarding the charge carrier separation due to the fast recombination and low diffusion length of the generated charge carriers.[20] Second, the mass transfer of MB molecules and degradation products might be limited due to the smaller pore diameter.

The ALD cycle number of deposited Fe_2O_3 also determines the photocatalytic activities of AAO-PhCs anodized by using a pulse period of 275 s (Figure 4). Similar to the samples anodized with 270 s pulse duration, surface roughness dominates the activity when comparing the AAO-PhC coated by 77 cycles Fe_2O_3 ($1.65 \pm 0.01\ h^{-1}$) to the sample functionalized with 154 cycles ($1.61 \pm 0.01\ h^{-1}$). Increasing the ALD cycle number to 231 raises the photocatalytic activity to $1.97 \pm 0.02\ h^{-1}$, which is probably caused by a combination of the film thickness increment and the alignment of the PSB to the semiconductor band gap. Since the PSB edge of the sample coated with 308 cycles does not overlap with the Fe_2O_3 absorption, the photocatalytic activity is lower ($1.72 \pm 0.04\ h^{-1}$) than in the previous sample. The deviation of the PSB blue edge from the Fe_2O_3 band gap can be explained by variations of the anodization parameters such as temperature or electrolyte volume. Nevertheless, this deviation demonstrates the importance of precisely aligning the PSB edge with the semiconductor band gap to use the slow photon effect. The AAO-PhC functionalized by 385 ALD cycles features the highest activity ($2.05 \pm 0.04\ h^{-1}$), as already observed in the AAO-PhCs produced by 270 s pulse duration. The PSB edge alignment enhances the photodegradation reaction by the slow photon effect. Apart from that, these AAO-PhCs' film thickness seems to be optimal regarding charge carrier generation, separation, and available pore diameter for mass transfer. Specifically, the generated charge carriers can induce MB photodegradation reactions before they vanish by recombination, which is a competitive process. Moreover, even though the AAO pore diameter is reduced by applying 385 Fe_2O_3 cycles in ALD, mass transfer of molecules taking part in the photoreaction within the pores is still possible to a sufficient amount. In contrast, further increase of the Fe_2O_3 thickness by using 462 ALD cycles reduces the AAO-PhCs' photocatalytic activity ($1.60 \pm 0.02\ h^{-1}$) due to increasingly hindered diffusion of reactants.

To sum up, the photocatalytic performance of Fe_2O_3-functionalized AAO-PhCs depends on the alignment of the PSB edge with the semiconductor band gap as well as on the deposited Fe_2O_3 film thickness. Precise control of the PSB edge position is crucial to enhance the photocatalytic activity by the slow photon effect. The Fe_2O_3 coating thickness needs to be optimized regarding the charge carrier dynamics and the mass transfer of molecules inside the AAO pores.

2.3. Photocatalytic Performance of Al_2O_3-Protected Fe_2O_3-AAO-PhCs

Ideal photocatalysts should not only have high initial activity, but this should also be maintained over multiple repetitions of the photocatalytic reactions. For Fe_2O_3, maintaining the photocatalytic properties is often challenging, since photocorrosion—also referred to as photodissolution—is a common issue.[11,53,54] This phenomenon describes the (partial) destruction of the material induced by irradiation utilized in photocatalytic processes to induce the charge carrier generation and, thereby, the reaction. To avoid this destruction of the structure and the corresponding decrease of its photocatalytic activity, the device has to be protected, for example, by coating another material on top.[11,53,54,94]

The photocatalytic activity of Fe_2O_3-coated AAO-PhCs decreases with an increasing number of photocatalysis measurements due to photocorrosion of the material. Still, it can be avoided when the structures are protected by ultra-thin layers of Al_2O_3, as shown in **Figure 5**. Repetition of photocatalysis measurements with AAO-PhCs anodized by employing 275 s pulse time and coated with 231 and 308 Fe_2O_3 cycles by ALD decreases the photocatalytic activity by 27% for both samples in their third measurements compared to the first ones (Figure 5a). This is probably caused by photocorrosion of the photocatalyst material, namely here Fe_2O_3, which has also been reported in previous publications.[54,93,95,96] A structural change at the surface of Fe_2O_3-AAO-PhCs is visible by SEM images taken after three photocatalysis measurements compared to the same sample before the first photocatalysis reaction (Figure 5b). As depicted in Figure 5c, the photocatalytic performance of AAO-PhCs functionalized with 385 cycles Fe_2O_3 can be stabilized when ultra-thin Al_2O_3 layers are coated on top by ALD. Within one ALD cycle, 1.4 ± 0.03 Å of Al_2O_3 is deposited. Although ultra-thin Al_2O_3 films of 2, 4, 6, and 8 cycles are used as protection layers, they can prevent the structural decomposition (Figure 5d), which was already shown in literature for similar applications.[55-60,97] The initial photocatalytic activity of Al_2O_3-protected Fe_2O_3-AAO-PhCs is lower than the unprotected one, but it remains constant for measurement repetitions and can outperform the unprotected structures after four measurements. For better comparison, the photocatalytic activity in Figure 5c is given as a percentage relative to the activity in the first measurement of the sample without the Al_2O_3 protection layer. With an increasing number of Al_2O_3 ALD cycles, the initial photocatalytic performance of the AAO-PhCs decreases and saturates at 54% (6 and 8 cycles). However, these activities are stable over three measurements in contrast to the sample without protective layer. Since the Fe_2O_3-AAO-PhC protected by 2 ALD cycles of Al_2O_3 features the highest initial activity of 67% when comparing the different numbers of Al_2O_3 ALD cycles, it was further used to test its performance over measurement repetitions compared to the unprotected sample. While the activity of the latter one is significantly decreasing with increasing measurement number by 44%, there is only a slight decrease of 4% in the activity of the structure protected by 2 ALD cycles. Furthermore, the absolute activity of the Fe_2O_3-AAO-PhC coated with 2 ALD cycles of Al_2O_3 is higher than that of the unprotected one from the fourth measurement onwards. Accordingly, an ultra-thin Al_2O_3 protection layer can stabilize the photocatalytic performance of Fe_2O_3-AAO-PhCs over multiple measurements by preventing photocorrosion of the photocatalytically active material. Since this stabilization is shown to be effective in terms of avoiding an activity decrease within six measurements, it is expected that the samples will be stable over multiple tests. Here it should be mentioned that, in contrast to the unprotected

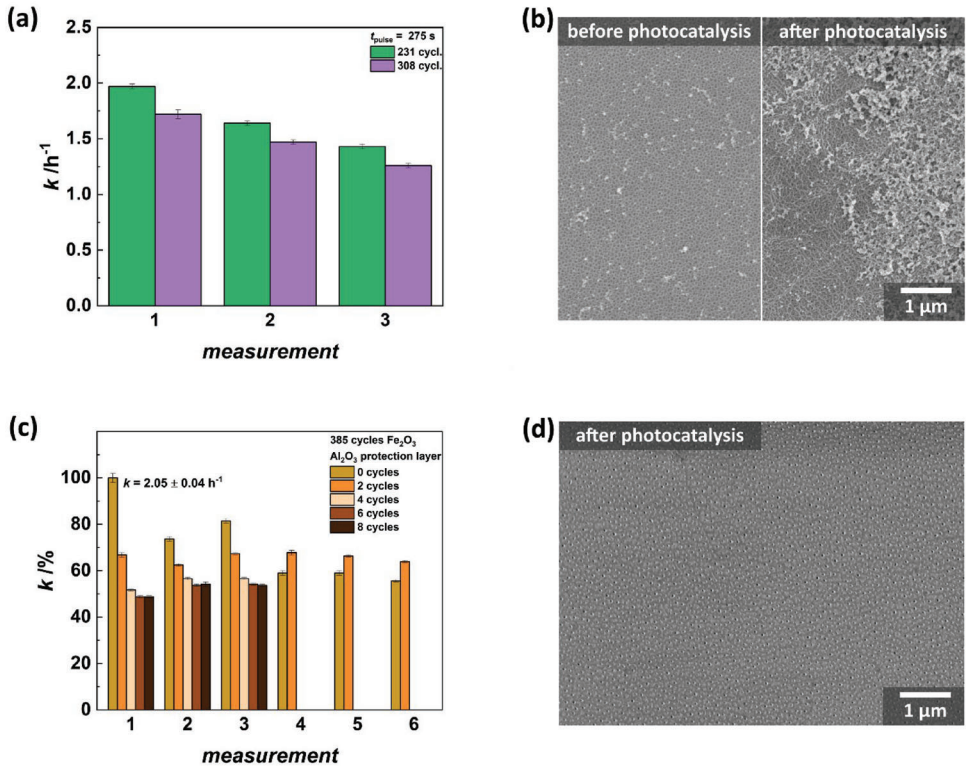

Figure 5. Photocorrosion and stabilized photocatalytic activity after depositing ultra-thin protection layers by ALD. a) The photocatalytic performance of AAO-PhCs functionalized with different ALD cycle numbers decreases with increasing measurement numbers due to photocorrosion of the Fe_2O_3 films. b) SEM images of the structures' top surface before and after photocatalysis measurements demonstrate structural changes of the sample. c) Protection of Fe_2O_3-AAO-PhCs by ultra-thin layers of Al_2O_3 by ALD stabilizes their photocatalytic performance over increasing measurement numbers. Although the initial activity is decreased compared to the unprotected structure, coating only 2 cycles of Al_2O_3 onto the structure outperforms the bare Fe_2O_3-AAO-PhC after four measurements. d) The SEM image of the sample protected by 2 cycles of Al_2O_3 was taken after photocatalysis measurements and showed no sample destruction at the surface.

Fe_2O_3-AAO-PhC, Photo-Fenton reactions can be suppressed on the Al_2O_3-protected sample since less iron ions are present at the samples' surface.[4] This might contribute to the observed reduction of the initial photocatalytic activity since the Photo-Fenton reaction would be beneficial for the overall apparent photocatalytic activity.

2.4. Photocatalytic Activity Enhancement for Degradation of Different Dyes

Fe_2O_3-AAO-PhCs with the PSB edge aligned with the Fe_2O_3 band gap possess a generally enhanced photocatalytic activity for photodegradation of different organic dyes, which is found to be independent of the model organic absorption characteristics. In contrast, existing literature reports mostly of titanium dioxide functionalized AAO-PhCs for photocatalytic decomposition of organic molecules (dyes and colorless compounds) using structures with the PSB edge aligned with one specific dye.[29,44,45,85]

As presented in **Figure 6**, the photocatalytic performance of AAO-PhCs with the PSB edge aligned to the Fe_2O_3 band gap and coated with the optimized semiconductor layer, i.e., 385 cycles of Fe_2O_3 and 2 cycles of Al_2O_3, features an increased activity compared to their uncoated counterparts for all three dyes. Depending on the dye, different activity enhancements by the factors 1.11 (MB), 1.49 (RhB), and 1.35 (MO) are observed. The slow photon effect can be effectively used for the photodegradation of all compounds because it is solely related to the Fe_2O_3-AAO-PhCs structure and materials. The activity enhancement also becomes clear when comparing the percentage removal of the dyes by the coated sample with the uncoated one. The uncoated sample decomposes 61 ± 2% of MB, 21 ± 2% RhB, and 16 ± 2% MO within one hour of reaction under the conditions used herein. The optimized Al_2O_3-protected Fe_2O_3-AAO-PhC shows dye removal of 68 ± 2% for MB, 29 ± 2% for RhB, and 22 ± 2% for MO. When the activity increase is based on the adjustment of the AAO-PhCs' PSB edge with the absorption of an organic molecule, the slow photon effect will only work for degrading these specific molecules. In Figure 6, such properties are observed for the Fe_2O_3-AAO-PhC with its PSB edge overlapping the absorption maximum of MB. For degrading MB, the photocatalytic performance of the Fe_2O_3/Al_2O_3 functionalized sample is enhanced compared to the pristine sample by a factor of 1.07 due to the slow photon effect. The performance is only slightly increased because the PSB red edge overlaps with the MB absorption maximum, thus causing screening of incoming light by the MB molecules. As expected, no activity increase can be observed for decomposing RhB because the optical properties of the dye and the PhC structure

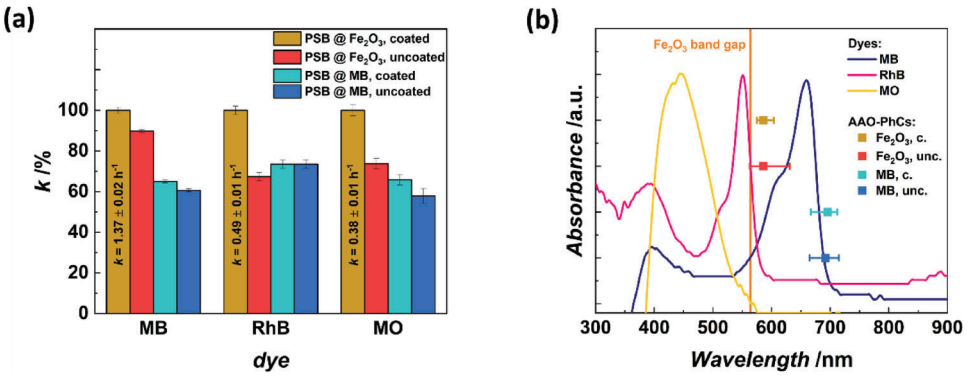

Figure 6. The degradation of different organic dyes as model pollutants of water demonstrates the general activity enhancement by the slow photon effect when the PSB of AAO-PhCs is aligned with the band gap of the semiconductor photocatalyst. The Fe_2O_3-functionalized samples are coated by 385 cycles of Fe_2O_3 and 2 cycles of Al_2O_3. a) Fe_2O_3-functionalized AAO-PhCs with the PSB edge matching the Fe_2O_3 band gap show significantly enhanced photocatalytic performance for degrading different organic dyes compared to the uncoated AAO-PhC structure. Only minor differences are observed for AAO-PhCs featuring a PSB edge at the absorption maximum of methylene blue. Note that the percent activity normalized to the photocatalytic activity of the coated sample with the PSB edge located at the Fe_2O_3 band gap is compared. The quantitative values of the activity for this sample are displayed for the different dyes. b) Absorbance spectra of the other organic dyes show the spectral alignment of the AAO-PhCs' PSB characteristics with respect to the different dyes and the band gap of Fe_2O_3. The labeling of the AAO-PhCs denotes the PSB edge position (at the Fe_2O_3 band gap or at the MB absorption) and whether the structure is coated with Fe_2O_3 (c.) or not (unc.).

do not match at all. The difference in the photocatalytic performance for the MO degradation of the coated AAO-PhC compared to its uncoated counterpart is within the measurement accuracy as the overall absolute activity is much lower than for the other dyes. Such small concentration changes are within the statistical error associated with the detector used in the UV–vis measurement. Moreover, calculations of the dye removal rates demonstrate that there is no significant difference between the Fe_2O_3-functionalized AAO-PhC and the uncoated sample when the PSB edge overlaps with the absorption of MB. Specifically, the functionalized sample is capable of degrading 46 ± 2% MB, 22 ± 2% RhB, and 14 ± 2% MO while the uncoated AAO-PhC decomposes 43 ± 2% MB, 21 ± 2% RhB, and 15 ± 2% MO within one hour.

The photocatalytic activity enhancement for degrading different organic compounds with the same Fe_2O_3-AAO-PhC proves that aligning the PSB edge with the semiconductor band gap results in a generally applicable slow photon effect, which is independent of the molecules to be degraded. The herein presented results of Fe_2O_3-AAO-PhCs are phenomenological in agreement with similar previously reported types of PhC structures, namely Fe_2O_3 inverse opals[92,98] and TiO_2-functionalized AAO-PhCs.[80] Furthermore, our study demonstrates the combination of Fe_2O_3 as a low-cost, visible light active photocatalyst with AAO-PhCs as widely tailorable template structures.

3. Conclusion

Fe_2O_3-AAO-PhCs were fabricated by combining pulsed aluminum anodization with ALD. The structures' optical and photocatalytic properties were systematically investigated by varying the period duration of the pulse-like anodization and the number of ALD cycles for Fe_2O_3 deposition by ALD. Optimized structures with the PSB edge overlapping with the semiconductor band gap were tested with further photocatalysis measurements and additional ultra-thin coatings of Al_2O_3 were applied as protective layers.

Previous literature reports mostly matched a PSB edge of AAO-PhCs with the absorption maximum of one chemical to be degraded. This approach facilitates the excitation of molecules of the respective chemical adsorbed at the AAO-PhCs surface by the slow photon effect. However, there is no activity increase for photocatalytic decomposition of different compounds when the PSB edge positions do not match their absorption profile. In contrast, we have demonstrated a general photocatalytic activity enhancement of semiconductor functionalized AAO-PhCs for degrading various organic compounds when the PhCs' PSB edge is aligned with the band gap of a semiconductor in the visible range of the electromagnetic spectrum. This activity enhancement is caused by the slow photon effect in the PhC structure, i.e., stimulated excitation of the semiconductor. Thus, it is independent of the chemical being degraded and its sensitivity to the PSB edge positions was shown. Moreover, Fe_2O_3 was first applied as a semiconductor coating for tailored AAO-PhCs and we proved an increased photocatalytic performance by employing the slow photon effect. The ALD-deposited Fe_2O_3 film thickness was optimized with respect to the structures' optical properties, charge carrier dynamics, and mass transfer of molecules within the porous structure to allow for high photocatalytic reaction rates. Furthermore, coating ultra-thin layers of Al_2O_3 onto the Fe_2O_3-AAO-PhC structures maintained the photocatalytic properties over multiple measurements and could avoid photocorrosion of the Fe_2O_3 film. Preparing Fe_2O_3-AAO-PhCs which feature higher absolute reflection intensities at their PSB might further increase the photocatalytic activity of these structures in the future as the interaction probability between incoming photons and the semiconductor will be further increased. Such higher reflection intensities can, for example, be realized by wet-chemical pore widening subsequent to the anodization of AAO-PhCs.[76,77]

Due to their pore structure, AAO-PhC samples could be fabricated as through-hole membranes by removing the remaining aluminum and opening the pore bottoms after anodization.[43,99] Such tailor-made through-hole AAO-PhC membranes functionalized with a semiconductor by ALD and aligned regarding their PSB edge position and band gap, respectively, might be utilized for water purification by filtration in combination with in situ photocleaning. Besides Fe_2O_3, ALD offers a large variety of cheap and earth-abundant photocatalysts to be deposited, such as titanium dioxide, zinc oxide, or tungsten oxide.[48] Coating AAO-PhCs with these materials or combinations of them might allow for even more efficient use of solar light for photocatalytic reactions. Moreover, the application of semiconductor-functionalized AAO-PhCs in photoelectrochemical processes could expand the utilization of such structures and provide low-cost and easy-to-manufacture material platforms for reactions such as water splitting.

4. Experimental Section

Materials: Aluminum (Al) chips (99.9997%, thickness 0.5 cm, 2 cm diameter) were purchased from Goodfellow GmbH (Germany). Oxalic acid ($H_2C_2O_4$), perchloric acid ($HClO_4$), ethanol (C_2H_5OH, EtOH), isopropyl alcohol (IPA), hydrochloric acid (HCl), copper (II) chloride dihydrate ($CuCl_2 \cdot 2\,H_2O$), nitric acid (HNO_3), methylene blue ($C_{16}H_{18}ClN_3S$, MB), rhodamine B ($C_{28}H_{31}ClN_2O_3$, RhB), methyl orange ($C_{14}H_{14}N_3NaO_3S$, MO), and hydrogen peroxide (H_2O_2) were supplied by Merck Chemicals (Germany) and used as received. Ferrocene ($C_{10}H_{10}Fe$, Cp_2Fe) was purchased from Alfa Aesar (Germany). Trimethylaluminum (C_3H_9Al, TMA) was received from Strem Chemicals (France). Milli-Q water (>16 MΩ cm, DI-H_2O) was used to prepare the aqueous solutions and as a precursor in the aluminum oxide ALD process.

Fabrication of AAO-PhCs: AAO-PhCs were produced by rectangular pulse anodization of Al under current density control conditions. Before anodization, the Al chips were cleaned for 30 min, respectively, in IPA and DI-H_2O and dried with a nitrogen stream. Afterward, electropolishing of the Al chips in 1:4 (v:v) solution of $HClO_4$ and EtOH was conducted for 3 min at 20 V and 5 °C. Anodization was carried out in 0.3 M $H_2C_2O_4$ aqueous solution at 6°C. The applied anodization profile began with a constant current period t_{const} for 60 min at a current density j_{const} of 4.2 mA cm^{-1} to initiate the formation of pores. Subsequently, 150 rectangular current pulses were applied. These consisted of alternating low and high current density levels j_{low} = 0.6 mA cm^{-1} and j_{high} = 4.2 mA cm^{-1} applied over the periods t_{low} and t_{high}, respectively. The low current density period was four times as long as the one of high current density, and the duration of one rectangular pulse t_{pulse} was calculated by the sum of t_{low} and t_{high}. The number of rectangular current pulses N_{rp} multiplied with the individual pulse duration t_{pulse} defined the total time over which the rectangular pulses were applied (t_{rp}). AAO-PhCs with different pulse durations, namely, 175, 270, 275, 300, 335, and 450 s, were anodized. After anodization, the AAO-PhC samples were washed with DI-H_2O and dried under nitrogen (N_2) flow. They were immersed into 30 wt.% H_2O_2 for 24 h, rinsed with DI-H_2O, and dried with N_2 stream.

ALD Coating of AAO-PhCs: ALD functionalization of AAO-PhCs was performed in a home-built ALD system operated under stop-flow conditions. Nitrogen (6.0, SOL) was used as carrier gas with a constant flow of 2.5 l h^{-1}. For depositing Fe_2O_3, the system temperature was 200 °C. Cp_2Fe heated to 130 °C and ozone (O_3) at room temperature (generated by an OzoneLab OL80W ozone generator; Ozone Services, Canada, from O_2 (5.0) by Westfalen) were used as precursors with pulse times of 1.5 s and 0.08 s, respectively. Exposure and pump times were 60 and 90 s during the Cp_2Fe half-reaction. In the O_3 half-reaction, exposure and pump durations of 30 and 90 s, respectively, were applied. Note, the O_3 half-reaction was repeated twice within one ALD cycle of Fe_2O_3 deposition to ensure sufficient O_3 diffusion within the reaction chamber without venting the system. The growth per cycle (GPC) for Fe_2O_3 deposition was 0.016 ± 0.003 nm. To functionalize the AAO-PhCs, 77, 154, 231, 308, 385, and 462 cycles were applied to achieve different film thicknesses.

ALD of Al_2O_3 was conducted at 150 °C system temperature utilizing TMA and DI-H_2O at room temperature as precursors. Both half-reactions consisted of 0.05 s precursor pulse, 60 s exposure, and 90 s pumping. The GPC was 0.14 ± 0.003 nm, and 2, 4, 6, or 8 cycles of Al_2O_3 deposition were conducted to generate an ultra-thin protection layer at the Fe_2O_3 coated samples with optimized film thickness.

The film thicknesses obtained within the respective ALD process were characterized by spectroscopic ellipsometry (SENpro ellipsometer, Sentech Instruments, Germany) on planar silicon reference substrates that were coated within the same ALD process as the AAO-PhCs. Atomic force microscopy (AFM) characterization of model Fe_2O_3 films was conducted using a Dimension 3100 Atomic Force Microscope (Bruker, USA) to determine the surface roughness of the films. The measurements were conducted on Fe_2O_3 films deposited onto silicon wafers applying ALD cycle numbers under the same conditions used in the study.

Optical Characterization: Optical characterization of AAO-PhCs was conducted by UV–vis spectroscopy in transmission and reflection using a Flame Extended Range Spectrometer (OceanOptics, Germany). Previously, the Al backsides of the AAO-PhC samples were removed by etching in a saturated $CuCl_2$/HCl solution. Only the Al area below the AAO was removed by defining it with a Kapton mask featuring a circular hole at the AAO position. Transmission spectra were measured in a home-built setup consisting of a deuterium-halogen light source DH-2000-BAL (OceanOptics, Germany), whose light was guided by a glass-fiber cable through a collimator to the sample, which was placed in normal incidence. The transmitted light was collected by a collimator and guided by a glass-fiber cable until it reached a Flame Extended Range Spectrometer (OceanOptics, Germany). Reflection measurements were conducted using the deuterium-halogen light source DH-2000, a glass-fiber cable, and the Flame Extended Range Spectrometer (OceanOptics, Germany) for data acquisition at normal incidence. The reflection measurements were conducted for AAO-PhCs filled with air and DI-H_2O. The spectral range for all measurements was 220 to 1020 nm with a resolution of 1 nm.

OriginPro 2021 software was used to analyze the PSB properties. The peak central wavelength was determined as PSB position by applying a Gaussian peak fit of the reflection data. To identify the PSB edges, the reflection data were smoothened using 200 data points, the second derivative was calculated, and the intersection points with the x-axis defined the PSB edge positions.

Photocatalytic Characterization: The photocatalytic activity of AAO-PhCs was studied by the degradation of organic dyes as model pollutants of water under simulated solar light irradiation. AAO-PhCs were mounted into a custom-built reaction chamber made of polyether ether ketone (PEEK) featuring a glass window for light irradiation. The sample was placed at normal incidence to a LE.5211 light source (Euromex Microscopen bv, Netherlands) generating visible-near infrared light (SI). The AAO-PhC was exposed to the solution inside the reaction chamber which was a mixture of 8 mL 2.5 mg L^{-1} dye solution and 200 mM H_2O_2. The solution was filled into the reaction chamber one hour before starting the photocatalysis measurement. The chamber was kept in darkness to enable adsorption-desorption equilibrium of the dye molecules at the AAO-PhC surface. Methylene blue, rhodamine B, and methyl orange were used as dyes featuring different absorption maxima, namely 664 nm (MB), 551 nm (RhB), and 446 nm (MO). After starting the illumination of the sample inside the dye solution, the absorbance of the reaction solution was measured by UV–vis spectroscopy every 5 min during 1 h total degradation time. A halogen light source HL-2000 (OceanOptics, Germany) and a Flame Extended Range Spectrometer (OceanOptics, Germany) were utilized for the UV–vis transmission measurement, whereby 1 mL of the reaction solution was pipetted into a cuvette, analyzed, and pipetted back into the reaction chamber. According to Lambert-Beer's law, the dye concentration is linearly proportional to its absorbance and can therefore be calculated after calibration with known concentrations. The dye degradation efficiency of AAO-PhCs was analyzed assuming Langmuir-Hinshelwood

kinetics, which typically describes photocatalytic reactions in heterogeneous phases. For diluted solutions (concentration smaller than 10^{-3} M), the Langmuir–Hinshelwood model could be simplified to pseudo-first-order kinetics and the apparent rate constant k was obtained from analyzing the concentration decrease over time (Equation 1):

$$\ln\left(\frac{c}{c_0}\right) = -k \times t \quad (1)$$

Here, the concentration of the dye after certain time steps is characterized by c, c_0 denotes the dye concentration at the beginning of the measurement ($t = 0$ h), and t is the reaction time.

Supporting Information

Supporting Information is available from the Wiley Online Library or from the author.

Acknowledgements

Authors would like to acknowledge funding by the Deutsche Forschungsgemeinschaft (DFG) within the Collaborative Research Initiative SFB 986 "Tailor-Made Multi-Scale Materials Systems" (project number 192346071). Spanish MCINN and AEI under research grant No. PID2019-108075RB-C32/AEI/10.13039/501100011033 are also gratefully acknowledged. Authors thank the support provided by the Australian Research Council through the grants DP200102614 and DP220102857. The authors acknowledge financial support from the Open Access Publication Fund of the Universität Hamburg.

Open access funding enabled and organized by Projekt DEAL.

Conflict of Interest

The authors declare no conflict of interest.

Data Availability Statement

The data that support the findings of this study are available from the corresponding author upon reasonable request.

Keywords

anodic aluminum oxide, atomic layer deposition, photocatalysis, photonic crystals, slow photon effect

Received: July 18, 2023
Revised: September 5, 2023
Published online: September 21, 2023

[1] M. A. Shannon, P. W. Bohn, M. Elimelech, J. G. Georgiadis, B. J. Mariñas, A. M. Mayes, *Nature* **2008**, *452*, 301.
[2] X. Qu, J. Brame, Q. Li, P. J. J. Alvarez, *Acc. Chem, Res.* **2013**, *46*, 834.
[3] The Sustainable Development Goals Report 2020, UN DESA, New York **2022**.
[4] R. S. Jack, G. A. Ayoko, M. O. Adebajo, R. L. Frost, *Environ. Sci. Pollut. Res.* **2015**, *22*, 7439.
[5] N. Kumar, S. Kumbhat, *Essentials in Nanoscience and Nanotechnology*, John Wiley & Sons Inc., Hoboken, New Jersey **2016**.
[6] W. Y. Teoh, J. A. Scott, R. Amal, *J. Phys. Chem. Lett.* **2012**, *3*, 629.
[7] M. B. Tahir, G. Nabi, M. Rafique, N. R. Khalid, *Int. J. Environ. Sci. Technol.* **2017**, *14*, 2519.
[8] Y. Zhang, Z. Jiang, J. Huang, L. Y. Lim, W. Li, J. Deng, D. Gong, Y. Tang, Y. Lai, Z. Chen, *RSC Adv.* **2015**, *5*, 79479.
[9] J. Zhang, P. Zhou, J. Liu, J. Yu, *Phys. Chem. Chem. Phys.* **2014**, *16*, 20382.
[10] O. Carp, *Prog. Solid State Chem.* **2004**, *32*, 33.
[11] J. Li, N. Wu, *Catal. Sci. Technol.* **2015**, *5*, 1360.
[12] J. Zhang, B. Tian, L. Wang, M. Xing, *Photocatalysis Fundamentals, Materials and Applications*, Springer Open Ltd, Singapore **2018**.
[13] R. L. Mckenzie, P. J. Aucamp, A. F. Bais, L. O. Björn, M. Ilyas, S. Madronich, *Photochem. Photobiol. Sci.* **2011**, *10*, 182.
[14] Y. Nam, J. H. Lim, K. C. Ko, J. Y. Lee, *J. Mater. Chem. A* **2019**, *7*, 13833.
[15] H. Chang, C. Su, C.-H. Lo, L.-C. Chen, T.-T. Tsung, C.-S. Jwo, *Mater. Trans.* **2004**, *45*, 3334.
[16] S. Shen, S. A. Lindley, X. Chen, J. Z. Zhang, *Energy Environ. Sci.* **2016**, *9*, 2744.
[17] P. Singh, K. Sharma, V. Hasija, V. Sharma, S. Sharma, P. Raizada, M. Singh, A. K. Saini, A. Hosseini-Bandegharaei, V. K. Thakur, *Mater. Today* **2019**, *14*, 100186.
[18] S. Grushevskaya, I. Belyanskaya, O. Kozaderov, *Materials (Basel)* **2022**, *15*, 4915.
[19] C. Xia, H. Wang, J. K. Kim, J. Wang, *Adv. Funct. Mater.* **2021**, *31*, 1.
[20] D. A. Wheeler, G. Wang, Y. Ling, Y. Li, J. Z. Zhang, *Energy Environ. Sci.* **2012**, *5*, 6682.
[21] D. H. Sliney, *Eye* **2016**, *30*, 222.
[22] O. Akhavan, *Appl. Surf. Sci.* **2010**, *257*, 1724.
[23] K. L. Hardee, A. J. Bard, *J. Electrochem. Soc.* **1977**, *124*, 215.
[24] J. K. Leland, A. J. Bard, *J. Phys. Chem.* **1987**, *91*, 5076.
[25] M. J. Kang, C. W. Kim, *Appl. Sci. Converg. Technol.* **2020**, *29*, 200.
[26] A. Trenczek-Zajac, M. Synowiec, K. Zakrzewska, K. Zazakowny, K. Kowalski, A. Dziedzic, M. Radecka, *ACS Appl. Mater. Interfaces* **2022**, *14*, 38255.
[27] J. I. L. Chen, G. Von Freymann, S. Y. Choi, V. Kitaev, G. A. Ozin, *J. Mater. Chem.* **2008**, *18*, 369.
[28] J. Liu, H. Zhao, M. Wu, B. Van Der Schueren, Y. Li, O. Deparis, J. Ye, G. A. Ozin, T. Hasan, B.-L. Su, *Adv. Mater.* **2017**, *29*, 1605349.
[29] S. Y. Lim, C. S. Law, M. Markovic, J. K. Kirby, A. D. Abell, A. Santos, *ACS Appl. Mater. Interfaces* **2018**, *10*, 24124.
[30] G. Guida, A. De Lustrac, A. C. Priou, *Prog. Electromagn. Res.* **2003**, *41*, 1.
[31] E. Yablonovitch, *J. Opt. Soc. Am. B* **1993**, *10*, 283.
[32] J. D. Joannopoulos, S. G. Johnson, J. N. Winn, R. D. Meade, *Photonic Crystals – Molding the Flow of Light*, Princeton University Press, Princeton, New Jersey **2008**.
[33] C. M. Soukoulis, *Nanotechnology* **2002**, *13*, 420.
[34] J. I. L. Chen, G. Von Freymann, S. Y. Choi, V. Kitaev, G. A. Ozin, *Adv. Mater.* **2006**, *18*, 1915.
[35] B. E. A. Saleh, M. C. Teich, *Fundamentals of Photonics*, John Wiley & Sons, Inc., Hoboken **2019**.
[36] J. F. Galisteo-López, M. Ibisate, R. Sapienza, L. S. Froufe-Pérez, Á. Blanco, C. López, *Adv. Mater.* **2011**, *23*, 30.
[37] S. Y. Lim, C. S. Law, L. Liu, M. Markovic, C. Hedrich, R. H. Blick, A. D. Abell, R. Zierold, A. Santos, *Catalysts* **2019**, *9*, 988.
[38] C. S. Law, S. Y. Lim, A. D. Abell, N. H. Voelcker, A. Santos, *Nanomaterials* **2018**, *8*, 788.
[39] A. Santos, *J. Mater. Chem. C* **2017**, *5*, 5581.
[40] B. Wang, G. T. Fei, M. Wang, M. G. Kong, L. De Zhang, *Nanotechnology* **2007**, *18*, 365601.
[41] A. M. Md Jani, D. Losic, N. H. Voelcker, *Prog. Mater. Sci.* **2013**, *58*, 636.
[42] A. Santos, M. J. Deen, L. F. Marsal, *Nanotechnology* **2015**, *26*, 042001.
[43] W. Lee, S.-J. Park, *Chem. Rev.* **2014**, *114*, 7487.

[44] S. Y. Lim, C. S. Law, M. Markovic, L. F. Marsal, N. H. Voelcker, A. D. Abell, A. Santos, *ACS Appl. Energy Mater.* **2019**, *2*, 1169.
[45] S. Y. Lim, C. S. Law, L. Liu, M. Markovic, A. D. Abell, A. Santos, *Catal. Sci. Technol.* **2019**, *9*, 3158.
[46] S. Y. Lim, C. Hedrich, L. Jiang, C. S. Law, M. Chirumamilla, A. D. Abell, R. H. Blick, R. Zierold, A. Santos, *ACS Catal.* **2021**, *11*, 12947.
[47] S. C. Riha, M. J. Devries Vermeer, M. J. Pellin, J. T. Hupp, A. B. F. Martinson, *ACS Appl. Mater. Interfaces* **2013**, *5*, 360.
[48] S. M. George, *Chem. Rev.* **2010**, *110*, 111.
[49] C. Bae, H. Shin, K. Nielsch, *MRS Bull.* **2011**, *36*, 887.
[50] M. Knez, K. Nielsch, L. Niinistö, *Adv. Mater.* **2007**, *19*, 3425.
[51] V. Cremers, R. L. Puurunen, J. Dendooven, *Appl. Phys. Rev.* **2019**, *6*, 021302.
[52] S. N. Ahmed, W. Haider, *Nanotechnology* **2018**, *29*, 342001.
[53] B. Weng, M.-Y. Qi, C. Han, Z.-R. Tang, Y.-J. Xu, *ACS Catal.* **2019**, *9*, 4642.
[54] S. Chen, D. Huang, P. Xu, W. Xue, L. Lei, M. Cheng, R. Wang, X. Liu, R. Deng, *J Mater Chem A Mater* **2020**, *8*, 2286.
[55] M. Leskela, E. Salmi, M. Ritala, *Mater. Sci. Forum* **2017**, *879*, 1086.
[56] J. Lu, J. W. Elam, P. C. Stair, *Acc. Chem. Res.* **2013**, *46*, 1806.
[57] W.-J. Lee, S. Bera, H. Woo, H. G. Kim, J.-H. Baek, W. Hong, J.-Y. Park, S.-J. Oh, S.-H. Kwon, *Chem. Mater.* **2022**, *34*, 5949.
[58] Y. S. Jung, A. S. Cavanagh, L. A. Riley, S.-H. Kang, A. C. Dillon, M. D. Groner, S. M. George, S.-H. Lee, *Adv. Mater.* **2010**, *22*, 2172.
[59] I. D. Scott, Y. S. Jung, A. S. Cavanagh, Y. Yan, A. C. Dillon, S. M. George, S.-H. Lee, *Nano Lett.* **2011**, *11*, 414.
[60] M. Liu, X. Xie, L. Chen, X. Wang, Y. Cheng, F. Lu, W.-H. Wang, J. Yang, X. Du, J. Zhu, H. Liu, H. Dong, W. Wang, H. Liu, *J. Mater. Sci. Technol.* **2016**, *32*, 489.
[61] J. Rasmussen, *Plat. Surf. Finish.* **2002**, *89*, 43.
[62] J. O'Sullivan, G. Wood, *Proc. Roy. Soc. Ser. A: Math. Phys. Sci.* **1970**, *317*, 511.
[63] W. Lee, R. Scholz, U. Gösele, *Nano Lett.* **2008**, *8*, 2155.
[64] M. M. Rahman, L. F. Marsal, J. Pallarès, J. Ferré-Borrull, *ACS Appl. Mater. Interfaces* **2013**, *5*, 13375.
[65] L. K. Acosta, F. Bertó-Roselló, E. Xifre-Perez, A. Santos, J. Ferré-Borrull, L. F. Marsal, *ACS Appl. Mater. Interfaces* **2019**, *11*, 3360.
[66] C. S. Law, S. Y. Lim, L. Liu, A. D. Abell, L. F. Marsal, A. Santos, *Nanoscale* **2020**, *12*, 9404.
[67] J. Lee, K. Bae, G. Kang, M. Choi, S. Baek, D.-S. Yoo, C.-W. Lee, K. Kim, *RSC Adv.* **2015**, *5*, 71770.
[68] W. J. Zheng, G. T. Fei, B. Wang, L. De Zhang, *Nanoscale Res. Lett.* **2009**, *4*, 665.
[69] P. Yan, G. T. Fei, G. L. Shang, B. Wu, L. De Zhang, *J. Mater. Chem. C* **2013**, *1*, 1659.
[70] T. Kumeria, A. Santos, M. M. Rahman, J. Ferré-Borrull, L. F. Marsal, D. Losic, *ACS Photonics* **2014**, *1*, 1298.
[71] T. Kumeria, M. M. Rahman, A. Santos, J. Ferré-Borrull, L. F. Marsal, D. Losic, *ACS Appl. Mater. Interfaces* **2014**, *6*, 12971.
[72] J. Ferré-Borrull, J. Pallarès, G. Macías, L. Marsal, *Materials (Basel)* **2014**, *7*, 5225.
[73] G. Macias, J. Ferré-Borrull, J. Pallarès, L. F. Marsal, *Nanoscale Res. Lett.* **2014**, *9*, 315.
[74] Y. Wang, Y. Chen, T. Kumeria, F. Ding, A. Evdokiou, D. Losic, A. Santos, *ACS Appl. Mater. Interfaces* **2015**, *7*, 9879.
[75] G. L. Shang, Y. Zhang, G. T. Fei, Y. Su, L. De Zhang, *Ann. Phys.* **2016**, *528*, 288.
[76] S. Y. Lim, C. S. Law, L. F. Marsal, A. Santos, *Sci. Rep.* **2018**, *8*, 1.
[77] C. S. Law, S. Y. Lim, A. D. Abell, L. F. Marsal, A. Santos, *Nanoscale* **2018**, *10*, 14139.
[78] C. S. Law, S. Y. Lim, A. Santos, *Sci. Rep.* **2018**, *8*, 4642.
[79] S. E. Kushnir, K. S. Napolskii, *Mater. Des.* **2018**, *144*, 140.
[80] L. Liu, S. Y. Lim, C. S. Law, B. Jin, A. D. Abell, G. Ni, A. Santos, *ACS Appl. Mater. Interfaces* **2020**, *12*, 57079.
[81] G. Szwachta, B. Januszewska, M. Wlodarski, M. Norek, *Appl. Surf. Sci.* **2023**, *607*, 155031.
[82] L. K. Acosta, F. Bertó-Roselló, E. Xifre-Perez, C. S. Law, A. Santos, J. Ferré-Borrull, L. F. Marsal, *ACS Appl. Mater. Interfaces* **2020**, *12*, 19778.
[83] L. Liu, S. Yee, C. Suwen, L. K. Acosta, B. Jin, A. D. Abell, L. F. Marsal, G. Ni, A. Santos, *Microporous Mesoporous Mater.* **2020**, *312*, 110770.
[84] W. Lee, J.-C. Kim, *Nanotechnology* **2010**, *21*, 485304.
[85] L. Liu, S. Y. Lim, C. S. Law, B. Jin, A. D. Abell, G. Ni, A. Santos, *J. Mater. Chem. A* **2019**, *7*, 22514.
[86] J. Ferré-Borrull, M. M. Rahman, J. Pallarès, L. F. Marsal, *Nanoscale Res. Lett.* **2014**, *9*, 416.
[87] B. I. Stefanov, B. S. Blagoev, L. Österlund, B. R. Tzaneva, G. V. Angelov, *Symmetry* **2021**, *13*, 1456.
[88] S. Haschke, Y. Wu, M. Bashouti, S. Christiansen, J. Bachmann, *ChemCatChem* **2015**, *7*, 2455.
[89] S. Schlicht, S. Haschke, V. Mikhailovskii, A. Manshina, J. Bachmann, *ChemElectroChem* **2018**, *5*, 1259.
[90] C. Argile, G. E. Rhead, *Surf. Sci. Rep.* **1989**, *10*, 277.
[91] M. Fondell, *Synthesis and Characterisation of Ultra Thin Film Oxides for Energy Applications*, Uppsala University, **2014**.
[92] H. Zhu, Y. Zhang, J. Zhu, Y. Li, S. Jiang, N. Wu, Y. Wei, J. Zhou, Y. Song, *J. Mater. Chem. A* **2020**, *8*, 22929.
[93] D. Beydoun, R. Amal, G. K. Low, S. Mcevoy, *J. Phys. Chem. B* **2000**, *104*, 4387.
[94] N. K. R. Eswar, S. A. Singh, J. Heo, *J. Mater. Chem. A* **2019**, *7*, 17703.
[95] D. Beydoun, R. Amal, G. Low, S. Mcevoy, *J. Mol. Catal. A: Chem.* **2002**, *180*, 193.
[96] M. I. Litter, M. A. Blesa, *Can. J. Chem.* **1992**, *70*, 2502.
[97] A. Paracchino, V. Laporte, K. Sivula, M. Grätzel, E. Thimsen, *Nat. Mater.* **2011**, *10*, 456.
[98] H. Xie, Y. Li, S. Jin, J. Han, X. Zhao, *J. Phys. Chem. C* **2010**, *114*, 9706.
[99] L. Zaraska, G. D. Sulka, M. Jaskula, *J. Solid State Electrochem.* **2011**, *15*, 2427.